Monthly Notices
of the
ROYAL ASTRONOMICAL SOCIETY

MNRAS **504,** 731–743 (2021)
Advance Access publication 2021 April 05

doi:10.1093/mnras/stab926

Metals and a search for molecules in the distant Universe: Magellan MIKE observations of sub-DLAs at $2 < z < 3$

Suraj Poudel [1,2★] Varsha P. Kulkarni,[1] Debopam Som [3] and Céline Péroux [4,5]

[1]*Department of Physics and Astronomy, University of South Carolina, 712 Main Street, Columbia, SC 29208, USA*
[2]*Instituto de Fisica, Pontificia Universidad Catolica de Valparaiso, Av. Universidad 330, Curauma, Valparaiso, Chile*
[3]*Space Telescope Science Institute, 3700 San Martin Drive, Baltimore, MD 21218, USA*
[4]*European Southern Observatory, Karl-Schwarzschild-Strasse 2, D-85748 Garching bei Munchen, Germany*
[5]*Aix Marseille University, CNRS, CNES, LAM, F-13007 Marseille, France*

Accepted 2021 March 27. Received 2021 February 27; in original form 2020 September 25

ABSTRACT

We present abundance measurements of the elements Zn, S, O, C, Si, and Fe for four sub-DLAs at redshifts ranging from $z = 2.173$ to 2.635 using observations from the MIKE spectrograph on the Magellan telescope to constrain the chemical enrichment and star formation of gas-rich galaxies. Using weakly depleted elements O, S, and or Zn, we find the metallicities after the photoionization corrections to be $[S/H] = -0.50 \pm 0.11$, $[O/H] > -0.84$, $[O/H] = -1.27 \pm 0.12$, and $[Zn/H] = +0.40 \pm 0.12$ for the absorbers at $z = 2.173$, 2.236, 2.539, and 2.635, respectively. Moreover, we are able to put constraints on the electron densities using the fine structure lines of C II* and Si II* for two of the sub-DLAs. We find that these values are much higher than the median values found in DLAs in the literature. Furthermore, we estimate the cooling rate $l_c = 1.20 \times 10^{-26}$ erg s^{-1} per H atom for an absorber at $z = 2.173$, suggesting higher star formation rate density in this sub-DLA than the typical star formation rate density for DLAs at similar redshifts. We also study the metallicity versus velocity dispersion relation for our absorbers. Most of the absorbers follow the trend one can expect from the mass versus metallicity relation for sub-DLAs in the literature. Finally, we are able to put limits on the molecular column density from the non-detections of various strong lines of CO molecules. We estimate 3σ upper limits of $\log N(\mathrm{CO}, J = 0) < 13.87$, $\log N(\mathrm{CO}, J = 0) < 13.17$, and $\log N(\mathrm{CO}, J = 0) < 13.08$, respectively, from the non-detections of absorption from the $J = 0$ level in the CO AX 0–0, 1–0, and 2–0 bands near 1544, 1510, and 1478 Å.

Key words: ISM: abundances – galaxies: high-redshift – quasars: absorption lines – galaxies: star formation.

1 INTRODUCTION

Since molecular clouds, formed out of the cold neutral clouds, are the birthplaces of stars, neutral gas is key to the formation of stars and galaxies. Absorption lines in quasar spectra offer a promising tool to measure the chemical properties of neutral gas in distant galaxies. Based on the values of neutral hydrogen column densities, the quasar absorption-line systems are classified into different categories. Damped Lyman-alpha absorbers (DLAs) and sub-damped Lyman-alpha absorbers (sub-DLAs) are especially important as they provide most of the neutral gas required for star formation (e.g. Péroux et al. 2003a; Nagamine, Springel & Hernquist 2004a, b; Wolfe & Chen 2006). DLAs and sub-DLAs have high neutral hydrogen column densities $\log N_{\mathrm{H\,I}} \geq 20.3$ and $19.0 \leq \log N_{\mathrm{H\,I}} < 20.3$, respectively. Unlike the emission-line technique that samples only the bright or star-forming galaxies (SFGs), absorption-line technique selects galaxies independent of their brightness. In addition, DLAs/sub-DLAs are less affected by photoionization compared to the Lyman limit systems (LLSs). DLAs/sub-DLAs are thus better suited for estimating the metallicity and help to trace the cycling of metals and neutral gas in the interstellar medium (ISM) and the circumgalactic medium (CGM).

One can constrain the evolution of the comoving density of metals in the Universe by measuring the metallicities of DLAs/sub-DLAs with a wide range of redshifts spanning a variety of cosmic epochs (e.g. Kulkarni et al. 2007). Such studies of sub-DLA/DLA metallicity evolution have been carried out extensively in the past (e.g. Kulkarni & Fall 2002; Prochaska et al. 2003a; Kulkarni et al. 2005, 2007; Rafelski et al. 2012, 2014; Jorgenson, Murphy & Thompson 2013; Som et al. 2013, 2015; Quiret et al. 2016; Poudel et al. 2018, 2020; Poudel S. 2020). However, a great deal remains unknown about the role they play in star formation and galaxy formation. In fact, many sub-DLAs are known to be more metal-rich than typical DLAs, and may represent a different population of galaxies (e.g. Khare et al. 2007; Kulkarni et al. 2010). Therefore, DLAs and sub-DLAs may have different nucleosynthetic histories, and possibly exhibit different star formation rates. The higher average metallicity of sub-DLAs also suggests that they may have higher dust content and thus provide better conditions for the formation of molecules than DLAs.

Wolfe et al. (2004) reported that the star formation rates per unit area for DLAs are in the range of 10^{-3}–10^{-2} $M_\odot$ yr^{-1} kpc^{-2}. Their findings were based on measurements of C II* absorption in 45

★ E-mail: spoudel@email.sc.edu

Table 1. Summary of targets and observations.

Quasar name RA(J2000), Dec.(J2000)	z_{em}	z_{abs}	log N_{HI} (cm^{-2})	Exposure time (s)	Wavelength coverage (Å)	Spectral resolution (R)
J1106−1731	2.572	2.173	20.05 ± 0.10	7200	3500–9400	Red: 22 000
RA: 11:06:07.47; Dec.: −17:31:13.50		2.539	19.00 ± 0.12			Blue: 28 000
J1244+1129	3.153	2.635	19.50 ± 0.12	5400	3500–9400	Red: 22 000
RA: 12:46:40.37; Dec.: 11:13:02.93						Blue: 28 000
J1614+1448	2.548	2.236	19.75 ± 0.10	5400	3500–9400	Red: 22 000
RA: 16:14:58.34; Dec.: 14:48:36.97						Blue: 28 000

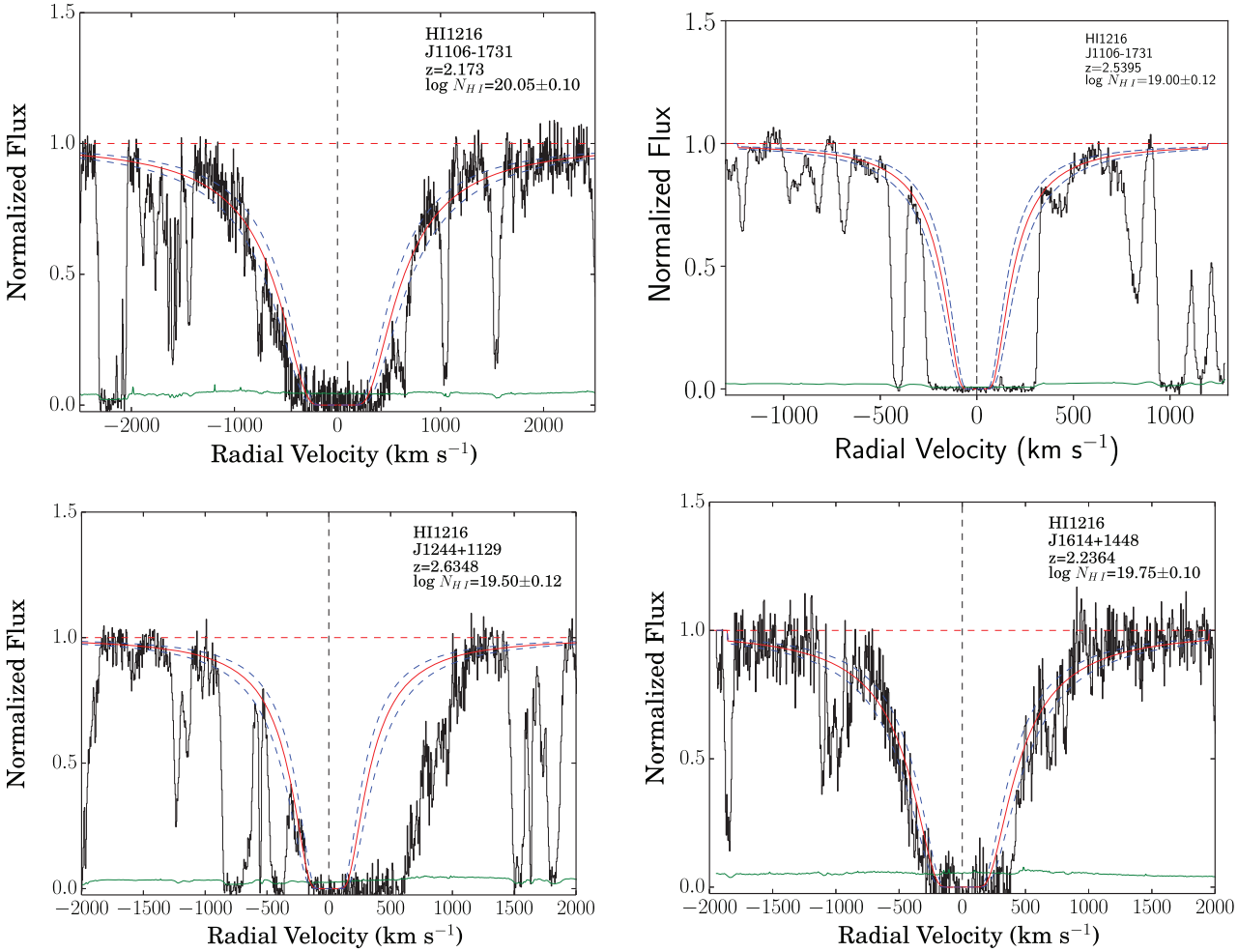

Figure 1. Plots showing the fitted Voigt profiles for hydrogen Ly α for each of our systems. In each case, observed data are shown in black, the solid curve in red shows the best-fitting profile with uncertainty in the fits shown by two dashed curves in blue. The continuum level spectrum is represented by the horizontal dashed line in red. The vertical dashed line in black corresponds to the redshift determined from the fits to the metal lines and the green curve at the bottom of each panel shows the 1σ error in the continuum-normalized flux. The names of the quasars, redshifts and log $N_{\rm H\,I}$ values of the absorbers are listed in the top right corner of each panel.

DLAs at redshifts $1.6 < z < 4.5$. However, these values remain largely unexplored for sub-DLAs. This is because most past studies in this field have focused on DLAs rather than sub-DLAs. It is interesting to note that sub-DLAs are in fact more abundant compared to DLAs: the differential $N_{\rm H\,I}$ distribution rises with decreasing $N_{\rm H\,I}$ (e.g. Zafar et al. 2013), and the number density of sub-DLAs integrated over their $N_{\rm H\,I}$ range exceeds that of DLAs (e.g. Noterdaeme et al. 2012). In spite of this, sub-DLAs have been ignored in many past studies of element abundances. This is because sub-DLAs often (though not always) have lower metal column densities in comparison to DLAs, which makes it necessary to have high spectral resolution and high signal-to-noise ratio (S/N) data to accurately determine their element abundances. High spectral resolution is also needed to resolve the C II* λ 1336 line without blending with the nearby C II λ 1334 line, which is usually strongly saturated. Moreover, study of the closely spaced molecular lines associated with the vibrational and rotational bands of H_2 and CO require high spectral resolution. The Magellan Inamori Kyocera Echelle (MIKE) spectrograph on the

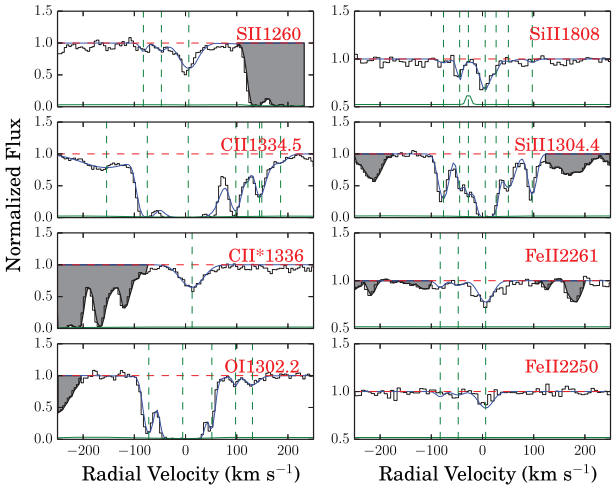

Figure 2. Plots showing Voigt profile fits for metal lines for the sub-DLA at $z = 2.173$ towards J1106−1731. In each panel, observed data are shown in black, the solid curve in blue shows the fitted profile, and the continuum level is represented by the horizontal dashed line in red. The vertical dashed lines in green are centred at the different velocity components, and the green line at the bottom of each panel shows the 1σ error in the continuum-normalized flux. The regions shaded in grey are caused by either telluric absorption or absorption from other systems not associated with the sub-DLA.

Magellan (Clay) telescope provides high enough resolution ($R \sim$ 22 000–28 000) to resolve the C II* λ 1336 as well as the molecular lines of CO.

Here, we present a study of the metallicities, electron densities, and cooling rate for a sample of four sub-DLAs observed at high resolution with the MIKE spectrograph on the Magellan (Clay) telescope. Moreover, we discuss the effect of photoionization on the derived abundances, search for the molecular lines, and put limits in the column densities of CO. In Section 2, we present details of our observations for the sub-DLAs and describe the data reduction process. In Section 3, we describe the technical aspects of spectroscopic measurements of absorption lines. The results for each of the sub-DLAs in our sample are presented in Section 4. In Section 5, we discuss various aspects of our results and compare them with the literature. Finally, in Section 6, we summarize our conclusions.

2 OBSERVATIONS AND DATA REDUCTION

Our sample consists of four absorbers with neutral hydrogen column densities ranging from $\log N_{\rm H\,I} = 19.00$ to 20.05, at redshifts 2.173–2.635 along the sightlines to three quasars. These quasars were observed with the MIKE spectrograph on the Magellan Clay telescope at Las Campanas observatory in Chile as a part of NOAO program 2010A-0499 (PI Kulkarni). Observations were carried out with the 1×5 arcsec^2 slit, which resulted in a spectral resolution of ∼22 000 with the red arm and ∼28 000 with the blue arm. While the blue arm has a wavelength coverage of 3400–4900 Å, the red arm has a wavelength coverage of 4900–9400 Å. The sightlines were observed in multiple exposures, to facilitate the rejection of cosmic rays. The details of the observations are summarized in Table 1.

The data reduction was performed using the standard MIKE pipeline reduction package. This code was developed by S. Burles, J. X. Prochaska and R. Bernstein and is written in IDL. The reduction package performs bias subtraction using the overscan region before flat-fielding the two-dimensional data. It then extracts individual spectral orders from the sky-subtracted flats. Wavelength calibration is done using exposures of a Th-Ar comparison lamp (which were obtained before and after each of the science exposures). This is followed by the correction to heliocentric velocities and the conversion from air wavelengths to vacuum wavelengths. Individual echelle orders were then extracted. Orders from multiple exposures were combined to reduce the effects of cosmic rays. Finally, the quasar continuum was fitted with a spline or Legendre polynomial (usually of order 4 or 5), and the spectra were normalized by this continuum fit.

3 VOIGT PROFILE FITTING AND ABUNDANCE MEASUREMENTS

We used the program VPFIT[1] v. 12.2 for fitting Voigt profiles to estimate column densities of all detected atoms and ions. VPFIT enables fitting of multicomponent Voigt profiles convolved with the instrumental profiles using multiple iterations. Moreover, VPFIT allows the Doppler b parameters and redshifts of the corresponding components to be tied together. All of our spectra have high enough resolution (10–14 km s^{-1}) to resolve the blending of metal lines. Although saturation can cause errors to the fitting results of individual lines, we reduced such errors by using multiple lines (e.g. Penprase et al. 2010). Most of the metal lines used for fitting are outside the Ly α forest and thus not affected by blending with hydrogen lines.

Ly α lines were fitted by fixing the redshifts as determined from the profile fits to the metal lines. The higher order Lyman series lines were not covered in most cases. Even when they were covered, they were blended with the Ly α forest features, and thus could not be used. To estimate the uncertainties in the H I column densities, we compared a series of fitted profiles with the observed data to make sure that the differences between the data and the fitted profiles do not exceed 2σ noise level. Using the H I and metal column densities, we next determined the abundances of all the observed elements following the standard definition,

$$[{\rm Y/H}] = \log(N_{\rm Y}/N_{\rm H\,I}) - \log({\rm Y/H})_{\odot}, \quad (1)$$

where $N_{\rm Y}$ and $N_{\rm H\,I}$ are the column densities for the element Y and neutral hydrogen, respectively. The last term $\log\,({\rm Y/H})_{\odot}$ is the abundance of the element Y in the Sun. Solar photospheric values were taken from Asplund et al. (2009). Finally, the rest-frame wavelengths and oscillator strengths of all the relevant transitions were adopted from Morton (2004) and Cashman et al. (2017).

4 RESULTS FOR INDIVIDUAL SUB-DLAS

In this section, we report the results for individual absorbers derived from Voigt profile fitting. We report the column densities of all detected atoms and ions, inferred absolute and relative abundances, and the gas kinematics determined from velocity dispersion measurements. For each system, the H I Ly α lines are shown in Fig. 1.

4.1 Sub-DLA at $z = 2.173$ towards J1106−1731

The sightline to J1106−1731 probes a sub-DLA at a redshift of $z = 2.173$. For this system, we determine the H I column density to be $\log N_{\rm H\,I} = 20.05 \pm 0.10$. We analysed the metal lines in this system by performing Voigt profile fitting for S II λ1260, Si II λ1808, Si II λ1304, Fe II λ2250, and Fe II λ2261. While the O I λ1302 and

[1] https://www.ast.cam.ac.uk/rfc/vpfit.html.

Table 2. Results from Voigt profile fitting in the $z_{abs} = 2.173$ sub-DLA towards J1106−1731.

z	b_{eff} (km s^{-1})	log $N_{O\,I}$	log $N_{Si\,II}$	log $N_{Fe\,II}$	log $N_{S\,II}$	log $N_{C\,II}$	log $N_{C\,II^*}$
2.172 627	5.54 ± 1.14		13.98 ± 0.03	13.98 ± 0.17	13.6 ± 0.20		
2.172 999	10.58 ± 2.09		14.72 ± 0.19	13.93 ± 0.21	13.7 ± 0.18		
2.173 208	9.17 ± 1.09		13.84 ± 0.03				
2.173 565	24.13 ± 1.63		14.98 ± 0.05	14.78 ± 0.04	14.58 ± 0.04		
2.173 781	3.31 ± 0.63		14.23 ± 0.16				
2.174 034	14.44 ± 2.65		13.86 ± 0.03				
2.174 408	6.26 ± 2.14		13.85 ± 0.04				
Total log N		>15.34	15.29 ± 0.06	14.89 ± 0.04	14.67 ± 0.04	>15.11	13.67 ± 0.20
[O/H]	[Si/H]	[Fe/H]	[S/H]	[Si/S]	[C/H]		
>−1.40	−0.27 ± 0.12	−0.66 ± 0.11	−0.50 ± 0.11	0.23 ± 0.06	>−1.37		

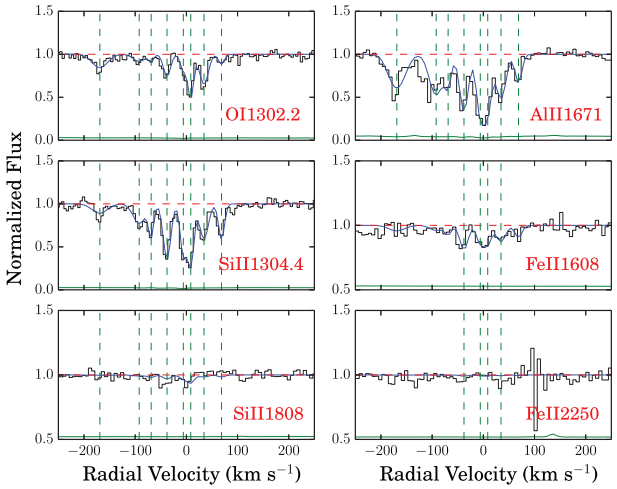

Figure 3. Same as Fig. 2 but showing the Voigt profile fits for the metal lines in the sub-DLA at $z = 2.539$ towards J1106−1731.

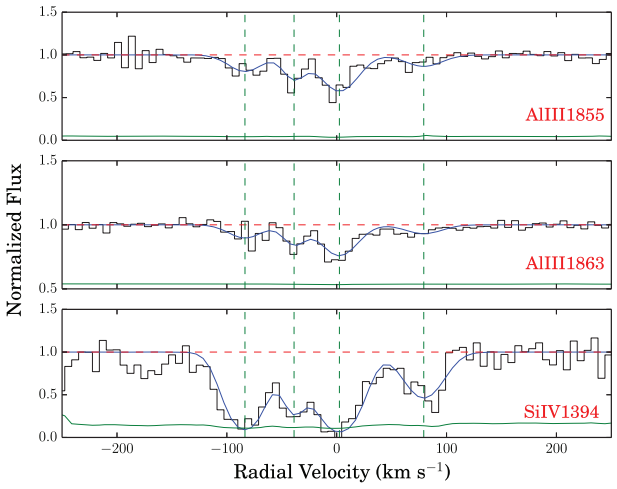

Figure 4. Same as Fig. 3 but showing the Voigt profile fits for the higher ions in the sub-DLA at $z = 2.539$ towards J1106−1731.

C II λ1334 lines were heavily saturated, we were able to estimate lower limits on O I and C II column densities. The C II* λ1336 line was also detected that, together with the lower limit on C II column density, allowed us to estimate the cooling rate as well as a limit on the electron density. Fig. 2 shows the Voigt profile fits for the metal lines, and the results from the fits are shown in Table 2. This system is a metal-rich sub-DLA with [S/H] = −0.50 ± 0.11.

4.2 Sub-DLA at $z = 2.539$ towards J1106−1731

The sightline to J1106−1731 probes a second sub-DLA at a redshift of $z = 2.539$. For this absorber, we determine the H I column density to be log $N_{H\,I} = 19.00 \pm 0.12$. We analysed this system by performing Voigt profile fitting for O I λ1302, Si II λ1304, Si II λ1808, Fe II λ1608, Fe II λ2250, Al II λ1671, Al III λ1855, Al III λ1863, and Si IV λ1394. Figs 3 and 4 show the Voigt profile fits for the lower and higher ions, respectively. The results from the fits are shown in Tables 3 and 4, respectively. This system has an ionization-corrected metallicity of [O/H]= −1.27 ± 0.12 (see Section 5.1 for details about ionization corrections).

4.3 Sub-DLA at $z = 2.635$ towards J1244+1129

The sightline to J1244+1129 probes a sub-DLA at a redshift of $z = 2.635$. For this absorber, we determine the H I column density to be log $N_{H\,I} = 19.50 \pm 0.12$. We performed Voigt profile fitting for O I λ1302, Si II λ1527, Fe II λ1608, Fe II λ2374, Al II λ1671, S II λ1260, Zn II λ2026.1, Zn II λ2062.7, Al III λ1855, Al III λ1863, and Si IV λ1394. Figs 5 and 6 show the Voigt profile fits for the detected atoms and ions. The results from the fits are shown in Tables 5 and 6. We note that Zn II λ2026.1 and Zn II λ2062.7 absorptions are very weak. However, the ionization-corrected value of [Zn/H] = 0.40 ± 0.12 is consistent with those of [O/H], [Si/H], and [Al/H] (see Table 10).

4.4 Sub-DLA at $z = 2.236$ towards J1614+1448

The sightline to J1614+1448 probes a sub-DLA at a redshift of $z = 2.236$. For this absorber, we determine the H I column density to be log $N_{H\,I} = 19.75 \pm 0.10$. We performed Voigt profile fitting for O I λ1302, Si II λλ 1304, 1808, Fe II λλ 1144, 1608, Al II λ 1671, Al III λ 1855, Al III λ 1863, Si II* λ1264, and Si II* λ1265. As Si II* λ1533 appears to be heavily blended with unrelated absorption, we fitted Si II* λ1264 and Si II* λ1265 together to estimate the Si II* column density. We used the column densities and Doppler parameters derived from fitting the Si II* λ1264 and Si II* λ1265 to compare the implied Si II* λ1533 profile with the data. The Si II* column density, together with the Si II column density, allowed us to put constraints on the electron densities. Figs 7–9 show the Voigt profile fits for the detected atoms and ions. The results from the fits are listed in Tables 7 and 8. This system is a fairly metal-rich sub-DLA with ionization-corrected metallicity of [O/H] > −0.84.

5 DISCUSSION

We now examine what implications our results have for various aspects of chemical enrichment processes for the ISM/CGM of

Table 3. Results from Voigt profile fitting in the $z_{abs} = 2.539$ sub-DLA towards J1106−1731.

z	b_{eff} (km s^{-1})	log $N_{O\,I}$	log $N_{Si\,II}$	log $N_{Fe\,II}$	log $N_{Al\,II}$
2.537 499	20.06 ± 2.09	13.58 ± 0.08	13.16 ± 0.11		12.40 ± 0.07
2.538 431	15.10 ± 2.14	13.18 ± 0.18	13.41 ± 0.06		12.41 ± 0.06
2.538 660	2.27 ± 0.14	12.82 ± 0.30	13.48 ± 0.11		12.19 ± 0.27
2.539 030	6.98 ± 2.14	13.50 ± 0.08	13.80 ± 0.03	13.24 ± 0.12	12.53 ± 0.08
2.539 411	4.16 ± 1.14	13.27 ± 0.10	13.75 ± 0.05	13.05 ± 0.19	12.85 ± 0.19
2.539 578	3.92 ± 1.14	13.87 ± 0.07	14.05 ± 0.08	13.08 ± 0.18	12.78 ± 0.21
2.539 893	9.11 ± 1.63	13.72 ± 0.06	13.55 ± 0.04	13.09 ± 0.16	12.35 ± 0.07
2.540 291	4.35 ± 1.14	13.04 ± 0.14	13.45 ± 0.06		12.06 ± 0.17
Total log N		14.39 ± 0.03	14.56 ± 0.03	13.72 ± 0.08	13.42 ± 0.07

Table 4. Results from Voigt profile fitting for different higher ions in the $z_{abs} = 2.539$ sub-DLA towards J1106−1731.

z	b_{eff} (km s^{-1})	log $N_{Al\,III}$	log $N_{Si\,IV}$
2.538 49	18.77 ± 1.14	12.46 ± 0.08	13.68 ± 0.11
2.539 02	10.90 ± 2.09	12.48 ± 0.07	13.22 ± 0.16
2.539 51	20.41 ± 1.63	12.90 ± 0.03	13.76 ± 0.12
2.540 41	21.3 ± 2.14	12.33 ± 0.11	13.22 ± 0.12
Total log N		13.20 ± 0.03	>14.14

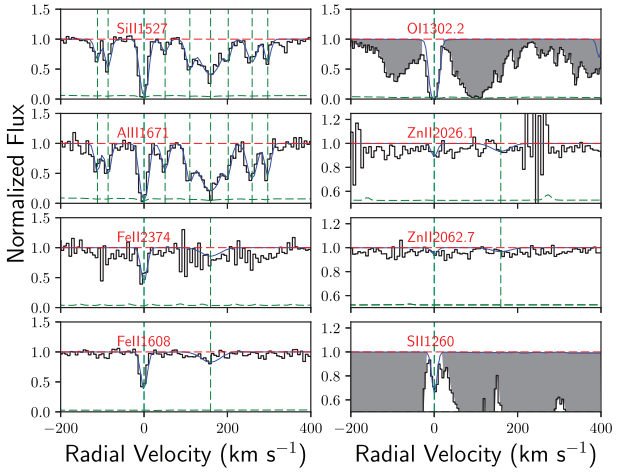

Figure 5. Same as Fig. 2 but showing the Voigt fits for metal lines for the sub-DLA at $z = 2.635$ towards J1244+1129.

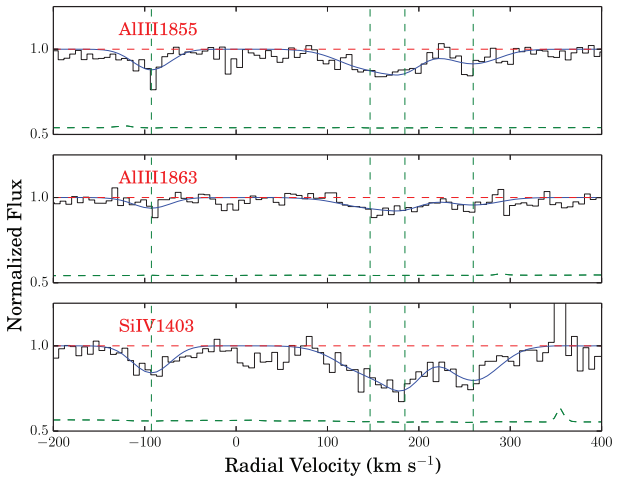

Figure 6. Same as Fig. 5 but showing the Voigt profile fits for the higher ions in the sub-DLA at $z = 2.635$ towards J1244+1129.

galaxies. We compare our results with those from the literature and discuss the trends in metallicity evolution, dust, relative abundances, and constraints on electron densities. Moreover, we discuss the photoionization, star formation rate density, and search for molecules in sub-DLAs.

5.1 Photoionization

Ignoring effects of ionization can lead to errors in the derived element abundances for the systems that consist of both neutral gas (H I regions) as well as ionized gas (H II regions). The low H I column density systems such as Lyman limit systems are heavily affected by the ionization effects. However, for high H I column density systems, ionization effects are either negligible or small (depending on the H I column density) due to the effect of self-shielding of ionizing photons. Therefore, in general, element abundances studies of DLAs ignore ionization corrections. For sub-DLAs, the H I column densities are much higher than LLSs, but smaller than for DLAs. Therefore, ionization corrections for sub-DLAs may not always be small enough to ignore. Past studies suggest that corrections to element abundances due to ionization are generally ≲0.2 dex for sub-DLAs (e.g. Dessauges-Zavadsky et al. 2003; Meiring et al. 2009; Cooke et al. 2011; Som et al. 2015). To assess the ionization corrections for three sub-DLAs in our sample, we ran the the plasma simulation code CLOUDY v. 13.03 (e.g. Ferland et al. 2013). For the sub-DLA at $z = 2.173$ that has relatively high H I column density (log $N_{H\,I} = 20.05 \pm 0.10$), we have not performed any photoionization corrections due to non-availability of higher ions to constrain the ionization parameter $U = n_\gamma/n_H$ (the ratio of the number density of ionizing photons to that of neutral hydrogen).

Each absorbing system is considered as a slab of uniform density that is heated by the cosmic microwave background (CMB) radiation and the extragalactic ultraviolet (UV) background radiation at the redshift of the absorber. The UV background, which plays an important role in the ionization state of intergalactic medium, was adopted from Khaire & Srianand (2019). These models use the latest values of quasar emissivity, star formation rate density of galaxies, dust attenuation, and the distribution of the intergalactic H I gas. In addition, the cosmic ray background was also included in our simulation. The observed Al III/Al II ratio was used to constrain the ionization parameter U for all the systems. In addition, for two cases, we also used the observed Si IV/Si II ratio.

For the system at $z = 2.539$ with log $N_{H\,I} = 19.00 \pm 0.12$, we used grids of models in the range $-1.0 >$ log $n_H > -3$, calculating the predicted column density ratio Al III/Al II. Comparing this prediction to the observed Al III/Al II ratio gave log $U = -2.49$ and log $n_H = -2.4$ (see Fig. 10). The resultant ionization corrections to be

Table 5. Results of Voigt profile fitting for different elements in the $z_{abs} = 2.635$ sub-DLA towards J1244+1129.

z	b_{eff} (km s^{-1})	log $N_{Si\,II}$	log $N_{Al\,II}$	log $N_{Fe\,II}$	log $N_{Zn\,II}$	log $N_{O\,I}$	log $N_{S\,II}$
2.633 463	3.10	13.27 ± 0.09	12.43 ± 0.15				
2.633 773	4.08	13.47 ± 0.07	12.41 ± 0.11				
2.634 817	5.37	15.18 ± 0.11	14.15 ± 0.16	14.00 ± 0.06	11.91 ± 0.15	>16.59	>14.08
2.635 429	6.71	12.95 ± 0.09	12.22 ± 0.07				
2.636 147	8.36	13.42 ± 0.05	12.42 ± 0.06				
2.636 751	29.3	13.95 ± 0.02	13.03 ± 0.02	13.62 ± 0.06	12.14 ± 0.14		
2.637263	3.66	13.10 ± 0.10	12.33 ± 0.13				
2.637 958	12.25	13.38 ± 0.04	12.50 ± 0.04				
2.638 413	3.83	13.29 ± 0.08	12.46 ± 0.11				
Total log N		>15.24	>14.23	14.15 ± 0.05	12.34 ± 0.02	>16.59	>14.08
[O/H]	[Si/H]	[Fe/H]	[Al/H]	[Zn/H]	[S/H]		
>0.40	>0.23	−0.85 ± 0.13	>0.28	0.28 ± 0.12	>−0.54		

Table 6. Results of Voigt profile fitting for different higher ions in the $z_{abs} = 2.635$ sub-DLA towards J1244+1129.

z	b$_{eff}$ (km s^{-1})	log $N_{Si\,IV}$	log $N_{Al\,III}$
2.633 693	27.15 ± 1.14	12.96 ± 0.08	12.37 ± 0.06
2.636 593	44.75 ± 1.63	13.19 ± 0.08	12.56 ± 0.07
2.637055	25.82 ± 2.14	13.02 ± 0.10	12.21 ± 0.12
2.637 961	37.34 ± 2.09	13.21 ± 0.06	12.34 ± 0.08
Total log N		13.71 ± 0.04	12.99 ± 0.04

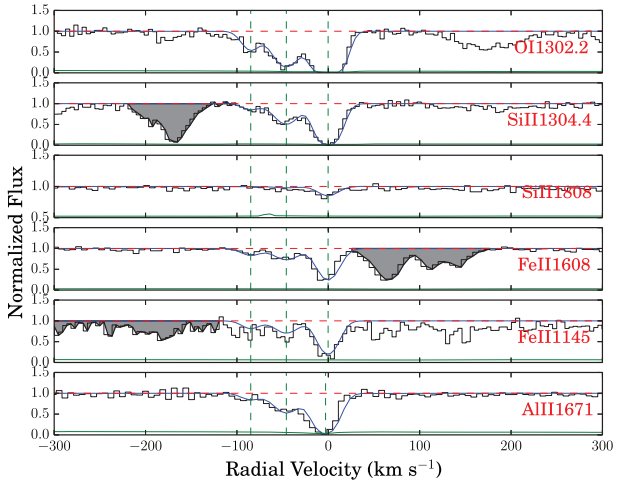

Figure 7. Same as Fig. 2 but showing the Voigt fits for the absorber at $z = 2.236$ towards J1614+1448.

applied is given as

$$\text{correction} = (\log\frac{N\,X_{\text{total}}}{N\,H_{\text{total}}} - \log\frac{N\,X_{\text{dominant ion}}}{\text{H I}}), \quad (2)$$

where X is an arbitary element, H_{total} = H I + H II, X_{total} = X I + X II + X III + ...) for various elements were then calculated. This implies ionization corrections of 0.03 dex for O, −0.87 dex for Si, −1.01 dex for Al, and −0.38 dex for Fe (see Table 9). The determination of the ionization correction for O was negligible (0.03 dex). This is understandable because the ionization potential of O I is nearly equal to that of H I. For the other elements, the corrections seem quite high, which is not surprising as this system is in the borderline of being a Lyman limit system and a sub-DLA. Moreover, the ionization parameter determined from the observed Si IV/Si II ratio was log U

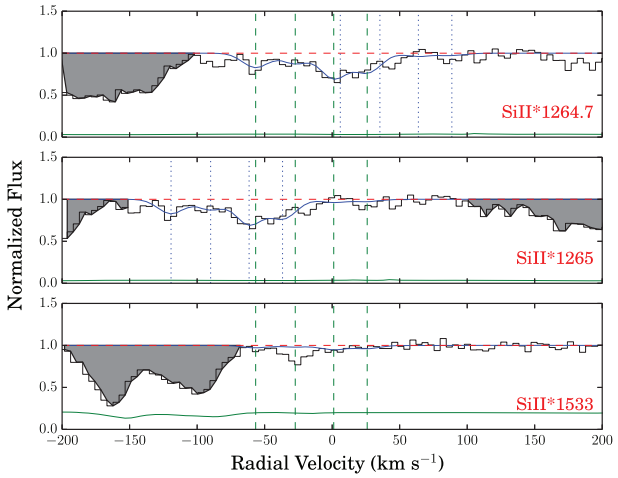

Figure 8. Velocity plots for Si II* λ1264.7, Si II* λ1265, and Si II* λ1533 lines for the absorber at $z = 2.236$ in the sightline to J1614+1448. The vertical dashed lines in green show the different velocity components included in the profile fits. The dotted lines in blue in the upper panel show the components corresponding to Si II* λ1265, and the dotted lines in blue in the middle panel show the components corresponding to Si II* λ1264.7. The absorption in the shaded regions are not associated with our system.

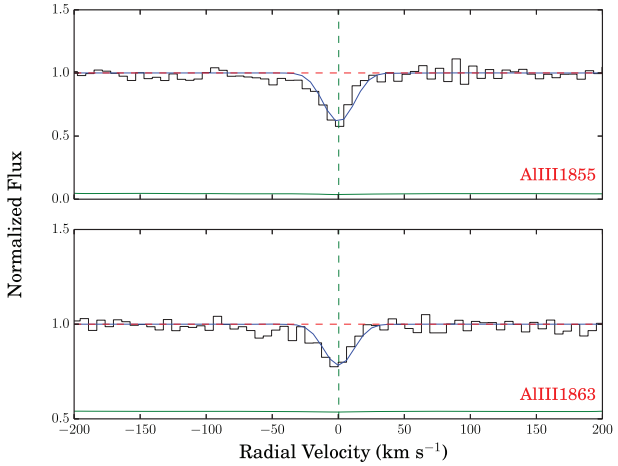

Figure 9. Same as Fig. 7 but showing the velocity plots for higher ions in the sub-DLA at $z = 2.236$ towards J1614+1448.

Table 7. Results of Voigt profile fits for elements in the $z_{abs} = 2.236$ sub-DLA towards J1614+1448.

z	b_{eff} (km s^{-1})	log $N_{Al\,II}$	log $N_{O\,I}$	log $N_{Si\,II}$	log $N_{Fe\,II}$	log $N_{Si\,II\star}$
2.235 47	11.43 ± 2.09	11.74 ± 0.27	13.94 ± 0.15	13.08 ± 0.29	13.28 ± 0.26	
2.235 89	15.79 ± 0.09	12.43 ± 0.22	14.55 ± 0.09	13.85 ± 0.08	13.62 ± 0.14	12.06 ± 0.28
2.236 24	11.49 ± 2.28					11.96 ± 0.34
2.236 39	11.42 ± 1.14					12.33 ± 0.18
2.236 87	12.29 ± 2.28	13.20 ± 0.25	15.56 ± 0.16	14.65 ± 0.08	14.21 ± 0.08	12.22 ± 0.22
Total log N		>13.28	>15.61	14.72 ± 0.07	14.35 ± 0.07	12.77 ± 0.12
[O/H]	[Si/H]	[Fe/H]	[Si/O]			
>−0.83	−0.54 ± 0.12	−0.90 ± 0.12	<0.29			

Table 8. Results of Voigt profile fits for higher ions in the $z_{abs} = 2.236$ sub-DLA towards J1614+1448.

z	b_{eff} (km s^{-1})	log $N_{Al\,III}$
2.236 344	13.21 ± 1.1	12.70 ± 0.02

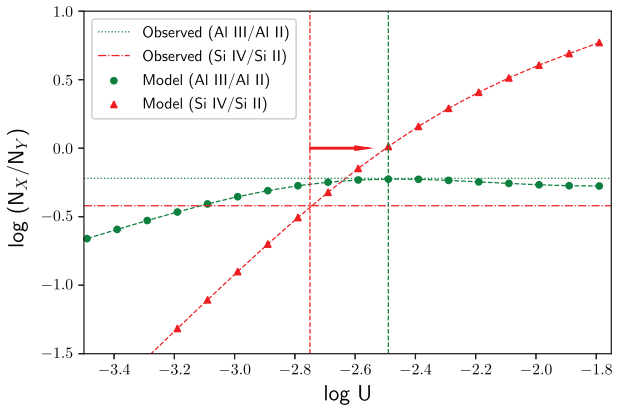

Figure 10. Results of Cloudy photoionization calculations for the absorber at $z = 2.539$ in the sightline to J1106−1731, showing the ion ratios as a function of the ionization parameter U. The vertical lines correspond to the value of U implied by the observed Si IV/Si II and Al III/Al II ratios (indicated by the horizontal lines in red and blue, respectively). The red arrow indicates that log U implied by the observed Si IV/Si II ratio is a limit consistent with the value determined from the observed Al III/Al II ratio.

> −2.75, which is consistent with the value determined from the observed Al III/Al II ratio.

For the system at $z = 2.635$ with log $N_{H\,I} = 19.50 \pm 0.12$, we used grids of models in the range 1.5 > log n_H > −3 to calculate the predicted column density ratios log Al III/Al II as well as log Si IV/Si II. Comparing the prediction to the observed Al III/Al II ratio gave log $U = -5.01$ and log $n_H = 0.1$ (see Fig. 11). The ionization corrections are quite small (∼±0.02 dex) for O, Si, Fe, and Al, and modest (0.12 dex) for Zn (see Table 10). Since Si II appears to be saturated, the ionization parameter constrained from log Si IV/Si II is log U <−3.1, which is consistent with the estimate from the observed Al III/Al II ratio. Similarly, for the system at $z = 2.236$ with log $N_{H\,I} = 19.75 \pm 0.10$, we used grids of models in the range 0.5 > log n_H > −3, calculating the predicted column density ratio log Al III/Al II. This gave log $U = -3.63$ and log $n_H = -1.2$ (see Fig. 12). The ionization corrections for this system are quite small (∼±0.1 dex for Si, and Fe) and the correction for O is again negligible (∼0.01 dex)(see Table 11). Since Al II appears saturated, the ionization parameters for both of these absorbers are likely to be lower than the values listed above and the corrections for absorbers are likely to be even smaller. The ionization corrections for all of these absorbers are listed in Tables 9–11. It is clear that the ionization corrections for the elements we use as metallicity indicators are either negligible (for O) or small (∼0.1 dex for Zn). These results are in agreement with past studies of ionization in sub-DLAs (e.g. Dessauges-Zavadsky et al. 2003; Meiring et al. 2009; Cooke et al. 2011; Som et al. 2015).

5.2 Metallicity, relative abundances, and dust

In general, the sub-DLA global mean metallicity seems to be higher than that of DLAs in the redshift range $0 \lesssim z \lesssim 3$ for which both DLA and sub-DLA observations are available (e.g. Som et al. 2013, 2015). As sulfur, oxygen, and zinc are weakly depleted on interstellar dust grains, they are believed to probe nearly dust-free or intrinsic metallicity. The zinc-based metallicity for the absorber at $z = 2.635$ along the sightline to J1244+1129 is supersolar ([Zn/H] $= 0.40 \pm 0.12$). Similarly, sulfur-based metallicity for the absorber at $z = 2.173$ along the sightline to J1106−1731 is [S/H] $= -0.50 \pm 0.11$. The oxygen-based metallicities for the absorbers at $z = 2.539$ and 2.236 along the sightlines to J1106−1731 and J1614+1448 are estimated to be [O/H] $= -1.27 \pm 0.12$ and [O/H] > −0.84, respectively. This shows that all of our 4 four sub-DLAs are found to be metal-rich based on the weakly depleted elements compared to typical DLAs at comparable redshifts.

Si and Fe are found to be underabundant relative to Zn, with [Si/Zn] > −0.19 and [Fe/Zn] $= -1.27$ for the absorber at $z_{abs} = 2.635$ along the sightline to J1244+1129. Similarly, Fe is found to be underabundant relative to S, with [Fe/S] $= -0.16$ for the absorber at $z_{abs} = 2.173$ along the sightline to J1106−1731. Such [Si/Zn], [Fe/Zn], and [Fe/S] values can be expected if the refractory elements (elements with higher condensation temperature) such as Si and Fe are depleted on to dust grains more severely than the volatile elements (elements with lower condensation temperature) such as Zn and S. However, it is interesting to note that the Si is overabundant in comparison to S for the absorber at $z = 2.173$, with [Si/S] $= 0.23 \pm 0.06$. Such a high [Si/S] value is very surprising, as [Si/S] is often either negative or zero depending on whether the dust depletion exists or not.

5.3 Gas kinematics

Ledoux et al. (2006), Møller et al. (2013), and Péroux et al. (2003a) reported a relation between velocity width versus metallicity of the absorption-line systems. The velocity width of absorption lines could be related to the gravitational potential well of the absorption system's host galaxy (e.g. Prochaska & Wolfe 1997; Haehnelt, Steinmetz & Rauch 1998; Pontzen et al. 2008) and may be taken as a proxy for the stellar mass. Thus, one potential interpretation

Table 9. Total and relative element abundances in the $z_{abs} = 2.539$ absorber along the sightline to J1106−1731, before and after ionization correction.

Element	$[X/H]_{NoIC}$	Correction	$[X/H]_{IC}$	$[X/O]_{NoIC}$	$[X/O]_{IC}$
O	-1.30 ± 0.12	$+0.03$	-1.27 ± 0.12		
Si	0.05 ± 0.12	-0.87	-0.82 ± 0.12	1.35 ± 0.04	0.45 ± 0.04
Fe	-0.78 ± 0.14	-0.38	-1.16 ± 0.14	0.52 ± 0.08	0.11 ± 0.08
Al	-0.03 ± 0.14	-1.01	-1.04 ± 0.14		

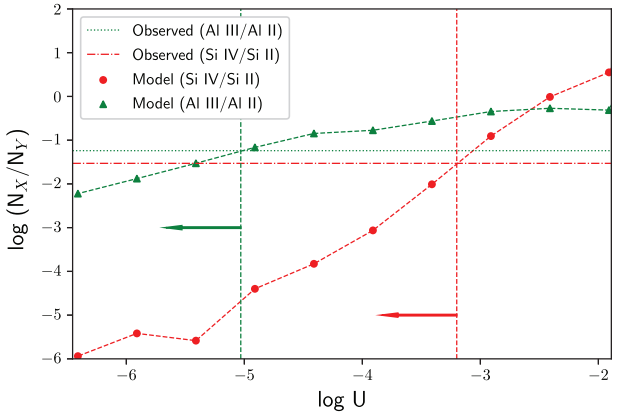

Figure 11. Same as Fig. 10 but showing the results of Cloudy photoionization calculations for the absorber at $z = 2.635$ in the sightline to J1244+1129. The red and green arrows indicate that log U implied by both the observed Si IV/Si II and Al III/Al II ratios are limits, suggesting that the ionization potentials would be even less than the values suggested by the vertical lines and the correction would be even smaller.

of the velocity width versus metallicity relation is in terms of the stellar mass versus metallicity relation (MZR) of galaxies, assuming galaxy luminosity scales with the dark matter halo mass. While many previous studies suggest a correlation between mass and metallicity, Zwaan et al. (2008) show that the velocity width and mass do not correlate well in local analogues of DLAs. We measured the velocity width values for the systems in our sample following the analysis of Wolfe & Prochaska (1998). The low-ionization transitions were used to measure the velocity width for all the systems. High-ionization lines are not appropriate as they are more likely to be dominated by large-scale thermal motions in the gas. Moreover, we selected only those transitions that are not so strong as to be affected by saturation, and at the same time, are not so weak as to be undetectable in some velocity components (so as to avoid underestimating the velocity widths). Figs 13, 14, 15, and 16 show the measurements of velocity widths for the systems at redshifts 2.173, 2.539, 2.236, and 2.635, respectively.

The Si II absorption lines in the $z_{abs} = 2.173$ and 2.236 sub-DLAs along the sightlines to J1106−1731 and J1614+1448 are spread over velocity widths of 157 and 69 km s^{-1}, respectively (Figs 13 and 15). The observed values of metallicities for these two systems are $\lesssim 2\sigma$ of the expected values based on the metallicity–velocity relation,

$$[X/H] = (0.88 \pm 0.08) \log \Delta V_{90} - (1.86 \pm 0.16), \quad (3)$$

observed for lower redshift sub-DLAs (Som et al. 2015). Similarly, the Fe II absorption for the $z_{abs} = 2.635$ sub-DLA along the sightline to J1244+1129 has a velocity width of 188.2 km s^{-1}, which is also consistent with the prediction from the metallicity–velocity relation (see Fig. 16). Moreover, the O I absorption in the $z_{abs} = 2.539$ sub-DLA along the sightline to J1106+1731 is spread over velocity width of 221 km s^{-1} (see Fig. 14). The metallicity of this absorber (-1.27 ± 0.12) is significantly lower than the value one can expect from the MZR relation for sub-DLAs from Som et al. (2015).

5.4 Constraints on electron densities

The collisional excitation of an electron to the higher energy state is followed by spontaneous radiative de-excitation. By assuming equilibrium between these two processes for a given temperature, fine structure lines such as Si II* λλ1264, 1265, 1533 and C II* λ 1335.7 can be used to put constraints on the electron density for an absorber (e.g. Srianand & Petitjean 2000). Si II* absorption is generally detected in gamma-ray burst (GRB) afterglows (e.g. Savaglio 2012). However, it is not very common in quasar absorbers. Only a few detections of Si II* exist in DLAs (e.g. Kulkarni et al. 2012; Noterdaeme et al. 2015). We detect Si II* absorption in the sub-DLA at $z_{abs} = 2.236$ along the sightline to J1614+1448. We performed Voigt profile fitting of Si II* λλ1264, 1265, 1533 simultaneously and determined log $N_{Si\,II^*}$ to be 12.77 ± 0.12. The Si II collisional excitation rate was assumed to be

$$C_{12} = 3.32 \times 10^{-7} (T/10^4)^{-0.5} \exp(-413.4/T)\ \mathrm{cm^3\ s^{-1}}, \quad (4)$$

and the Si II* spontaneous radiative de-excitation rate $A_{21} = 2.13 \times 10^{-4}$ s^{-1} (e.g. Srianand & Petitjean 2000). The electron density is then given by

$$n_e = (N_{Si\,II^*}/N_{Si\,II}) A_{21}/C_{12}. \quad (5)$$

As C_{12} depends on temperature, we estimate the electron densities at two different temperatures $T = 500$ and 7000 K. We obtained $n_e = 3.63$ cm^{-3} and 6.30 cm^{-3}, respectively, for $T = 500$ and 7000 K. These values are much higher than the median value $n_e = 0.0044 \pm 0.0028$ cm^{-3} found in DLAs (e.g. Neeleman, Prochaska & Wolfe 2015) and also higher than the range of electron density values (0.007–0.047 cm^{-3}) found in the H_2-bearing high-z DLAs (e.g. Srianand et al. 2005). In fact, our above-mentioned estimates of the electron density in the sub-DLA toward J1614+1448 are higher than even the values found in some super-DLAs (e.g. Kulkarni et al. 2012, 2015; Noterdaeme et al. 2015), the highest of which is in the range $n_e = 0.53$–0.91 cm^{-3}.

Moreover, we were able to detect C II* λ 1335.7 for the absorber at $z = 2.173$ in the sightline to J1106−1731. However, as most of the components of C II λ1334 were saturated for this system, we were able to put only an upper limit on the electron density, n_e. Again, we estimated the electron density,

$$n_e = (N_{C\,II^*}/N_{C\,II}) A_{21}/C_{12}, \quad (6)$$

by assuming equilibrium between the collisional excitation and the radiative de-excitation of C II, where, $A_{21} = 2.29 \times 10^{-6}$ s^{-1} (e.g. Nussbaumer & Storey 1981). The collision rate coefficient is given by

$$C_{12}(T) = [8.63 \times 10^{-6} \Omega_{12}/(g_1 T^{0.5})] \exp(-E_{12}/kT) \quad (7)$$

Table 10. Total and relative element abundances in the $z_{abs} = 2.635$ absorber along the sightline to J1244+1129, before and after ionization correction.

Element	$[X/H]_{NoIC}$	Correction	$[X/H]_{IC}$	$[X/O]_{NoIC}$	$[X/O]_{IC}$
O	>0.40	−0.004	>0.40		
Si	>0.23	−0.02	>0.21		
Fe	-0.85 ± 0.13	−0.02	-0.87 ± 0.13		
Al	>0.28	0.02	>0.30		
Zn	0.28 ± 0.12	0.12	0.40 ± 0.12		

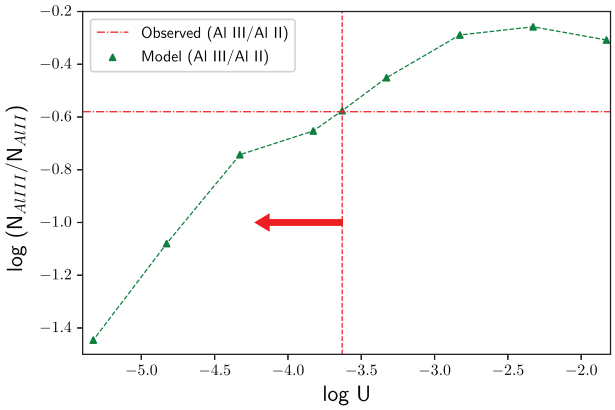

Figure 12. Same as Fig. 10 but showing the results of Cloudy photoionization calculations for the absorber at $z = 2.236$ in the sightline to J1614+1448. The red arrow indicates that log U implied by both the observed Al III/Al II ratio is a limit, suggesting that the ionization parameter would be less than the value suggested by the vertical line and the correction would be even smaller.

(e.g. Wood & Linsky 1997), where, $g_1 = 2$, $E_{12} = 1.31 \times 10^{-14}$ erg, and the collision strength Ω_{12} depends on temperature. We were able to put upper limits of $n_e < 0.18$ and $n_e < 0.58$ cm^{-3}, respectively, for $T = 500$ and 7000 K. These values are consistent with the median value $n_e = 0.0044 \pm 0.0028$ cm^{-3} found in DLAs (e.g. Neeleman et al. 2015).

5.5 Cooling rate

Wolfe, Gawiser & Prochaska (2003) developed a technique to infer the star formation rate per unit area for individual damped Ly α systems. In this technique, the [C II] 158-μm cooling rate is inferred from the C II λ1335.7 absorption line in the neutral gas producing the damped Ly α absorption. The C II* λ 1335.7 transition arises from the excited $^2P_{3/2}$ state in C^+. A spontaneous photon decay of the $^2P_{3/2}$ state to the $^2P_{1/2}$ state results in [C II] 158-μm emission, which is the principal coolant of neutral gas in the Galactic ISM (e.g. Wright 1991). At thermal equilibrium, the cooling rate equals the heating rate, which makes it possible to calculate the star formation rate per unit area. The cooling rate can be expressed as

$$l_c = \frac{N_{C\,II^\star} E_{ul} A_{ul}}{N_{H\,I}}, \quad (8)$$

where E_{ul} and A_{ul} denote the energy and coefficient for spontaneous photon decay for the transition from the $^2P_{3/2}$ state to $^2P_{1/2}$ (e.g. Pottasch, Wesselius & van Duinen 1979). Using $A_{ul} = 2.29 \times 10^{-6}$, we estimate $l_c = 1.20 \times 10^{-26}$ erg s^{-1} per H atom for the absorber at $z = 2.173$ in the sightline to J1106−1731, suggesting a higher star formation rate density in this sub-DLA than the typical star formation rate density for DLAs at similar redshifts from Wolfe et al. (2003). The cooling rate versus H I column density data for the sub-DLA from this work along with the corresponding measurements for DLAs from Wolfe et al. (2003), sub-DLAs from Som et al. (2013), and for interstellar clouds in the Milky Way adopted from Lehner, Wakker & Savage (2004) are plotted in Fig. 17. While our value of the cooling rate is lower than that for some other sub-DLAs and for low-velocity H I gas in the Milky Way ISM, it is higher than the cooling rate for all the DLAs from Wolfe et al. (2003).

5.6 Search for CO molecules

Most of the Lyman and Werner band absorption lines of H_2 for all the absorbers in our sample are not covered by the spectra. While a few of these lines are covered, the S/N in this region is very low and, furthermore, these lines are blended with the Ly α forest. For all of our absorbers, several lines of CO were covered, but they were not detected. We estimate 3σ upper limits of log N(CO, $J = 0$) < 13.87, log N(CO, $J = 0$) < 13.17, and log N(CO, $J = 0$) < 13.08, respectively, from the non-detections of absorption from the $J = 0$ level in the CO AX 0–0, 1–0, and 2–0 bands near 1544, 1510, and 1478 Å, respectively. These limits were calculated by estimating the average S/N per pixel adjacent to the expected positions of the molecular lines. Fig. 18 shows the velocity structures at the positions of the above-stated CO bands and Table 12 lists the corresponding 3σ upper limits on the CO column density for $J = 0$ from the non-detections of absorption from the $J = 0$ level in these bands. There is a slight hint of absorption in the CO A-X 0–0 band near 1544.45 Å for the $z = 2.635$ system, but no corresponding absorption (expected to be stronger) in the CO A-X 1–0 and 2–0 bands near 1509.75 and 1477.56 Å, respectively. Moreover, we made a rest-frame spectral stack of the four absorbers in order to increase the S/N and look for weak absorption. However, we do not notice any significant absorption, as seen in Fig. 19, which shows the velocity plots for the CO A-X 0–0, 1–0, and 2–0 bands near 1544, 1510, and 1478 Å, respectively, after making the rest-frame stacking.

CO absorption features in the background quasar provides an extremely useful tool to understand the chemical properties of the galaxies and to put constraints on fundamental physics (e.g. measuring the temperature of the cosmic microwave background radiation). However, detection of CO absorption remains extremely challenging as they require high-resolution and high S/N spectra to detect the weak and closely spaced rotational bands of CO. There exists only a handful of CO detections in the literature along the lines of sight to background quasars (e.g. Srianand et al. 2008; Noterdaeme et al. 2011, 2015, 2017, 2018). The upper limits of CO column densities for our absorbers are lower than most of the detections in the literature (see Fig. 20). This may be understandable as all of our systems have relatively low H I column densities and molecules are generally detected in high column density absorbers. The first detection of such kind was in a DLA at $z_{abs} = 2.4$ with log $N_{CO} = 13.89$ and log $N_{H\,I} = 20.10$ (e.g. Srianand et al. 2008). Similarly, Noterdaeme et al. (2017) reported a DLA at $z_{abs} = 2.4$ with

Table 11. Total and relative element abundances in the $z_{abs} = 2.236$ absorber along the sightline to J1614+1448, before and after ionization correction.

Element	$[X/H]_{NoIC}$	Correction	$[X/H]_{IC}$	$[X/O]_{NoIC}$	$[X/O]_{IC}$
O	>-0.83	-0.01	>-0.84		
Si	-0.54 ± 0.11	-0.15	-0.69 ± 0.11	<0.29	<0.15
Fe	-0.90 ± 0.12	-0.12	-1.02 ± 0.12	<-0.07	<-0.17
Al	>-0.92	0.09	>-0.83		

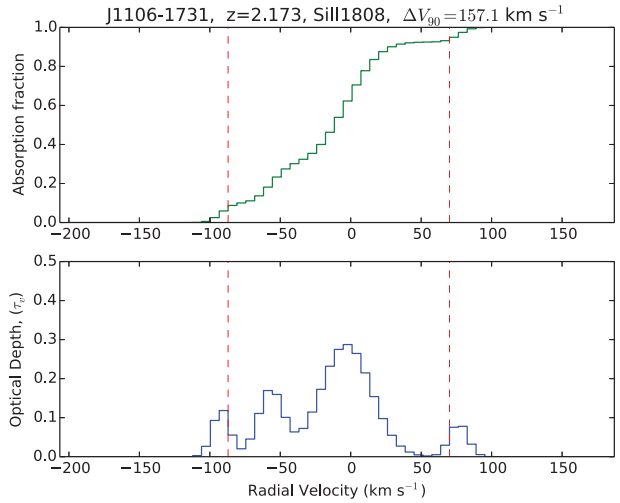

Figure 13. Upper panel: absorption fraction versus radial velocity. Lower panel: Optical depth versus radial velocity for the sub-DLA at $z_{abs} = 2.173$ towards J1106−1731. The top panel lists the name of the sightline, redshift of the sub-DLA, name of the transition used, and the corresponding velocity width. The velocity width is estimated as the radial velocity range that contains 90 per cent of the cumulative optical depth (i.e. the difference in radial velocity between the two vertical dashed lines in red drawn at 5 and 95 per cent of cumulative optical depth).

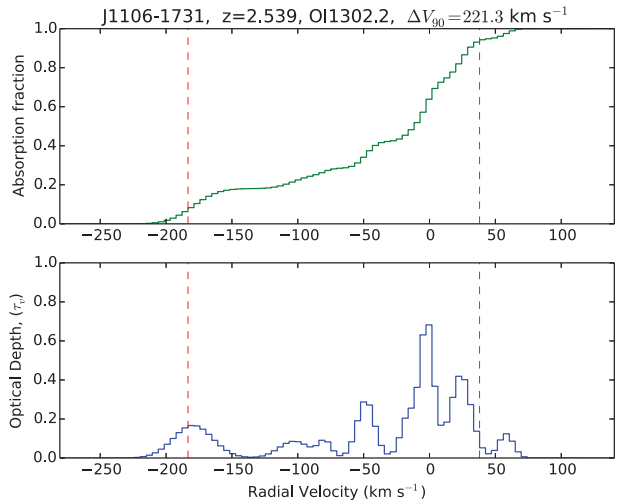

Figure 14. Same as Fig. 13 but for the sub-DLA at $z_{abs} = 2.539$ towards J1106−1731.

log $N_{CO} = 14.95$ and log $N_{H\,I} = 20.80$. Both of these systems have either near-solar or supersolar metallicities and depletion patterns similar to those in cold gas in the diffuse ISM. We also note that one of our systems at $z = 2.635$ that shows slight hint of absorption in the CO A-X 0–0 band near 1544.45 Å has similar metallicity and

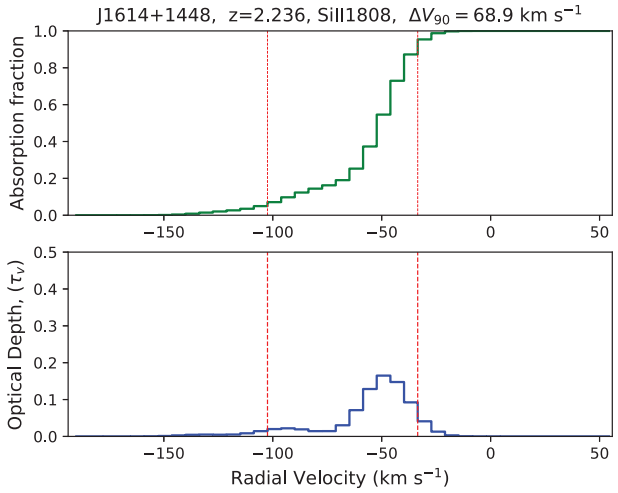

Figure 15. Same as Fig. 13 but for the sub-DLA at $z_{abs} = 2.236$ towards J1614+1448.

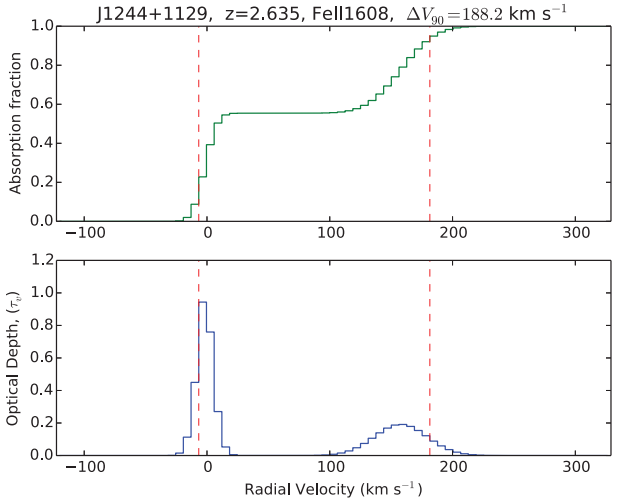

Figure 16. Same as Fig. 13 but for the sub-DLA at $z_{abs} = 2.635$ towards J1244+1129.

depletion level as the two systems in the literature. However, we can not confirm if this is truly an absorption from CO molecules as no hint of absorption can be seen in the stronger CO A-X 1–0 and 2–0 bands near 1509.75 and 1477.56 Å. Higher S/N and lower wavelength spectra of our sub-DLAs are essential to perform more sensitive searches for H_2 and CO.

6 CONCLUSIONS

In this paper, we have presented high-resolution absorption spectra of four sub-DLAs at $2.173 < z_{abs} < 2.635$, increasing the existing

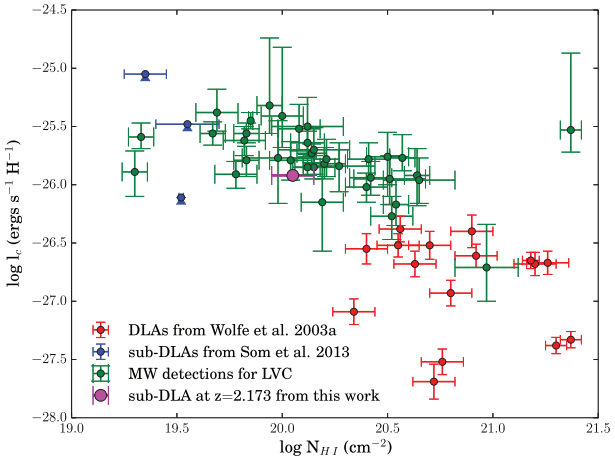

Figure 17. Cooling rate per H atom, l_c inferred from C II* column density, versus H I column density. The red points denote the sample of QSO DLAs in Wolfe et al. (2003). The green points represent the measurements for low-velocity interstellar H I clouds in the Milky Way compiled in Lehner et al. (2004). The point in magenta represents a sub-DLA at $z = 2.173$ along the sightline to J1106−1731 from this work. The blue points denote the lower limits for the sub-DLAs from Som et al. (2013).

sample for undepleted elements in sub-DLAs and thus improving the constraints on the cosmic metal evolution. We find a spread in the metallicities, which range from −1.27 to +0.40 dex. These observations suggest that metal-rich sub-DLAs appear at high redshift as well, supporting the conclusion made by Som et al. (2013). We are also able to put constraints on the electron density by assuming equilibrium between collisional excitation and spontaneous radiative de-excitation for an assumed gas temperature using fine-structure lines of C II* and Si II* for two of the sub-DLAs. These values are much higher than the values found in DLAs (including H_2-bearing DLAs) and even in super-DLAs. We estimate the cooling rate for a sub-DLA at $z = 2.173$ in the sightline to J1106−1731 using C II* λ1335.7 line to be $l_c = 1.20 \times 10^{-26}$ erg s^{-1} per H atom, suggesting higher SFR density in this sub-DLA than the typical SFR density for DLAs at similar redshifts. We also study the metallicity versus velocity dispersion relation for our absorbers and compare the values with those from the literature. Most of the absorbers follow the trend one can expect from the mass versus metallicity relation for sub-DLAs from literature. Finally, although our spectra either do not cover or have very low S/N in the locations of H_2 lines, we are able to put limits on the column density of CO from the non-detections of various strong electronic transitions. We estimate 3σ upper limits of $\log N(\mathrm{CO}, J = 0) < 13.87$, $\log N(\mathrm{CO}, J = 0) < 13.17$, and $\log N(\mathrm{CO}, J = 0) < 13.08$, respectively, from the non-detections of absorption from the $J = 0$ level in the CO AX 0–0, 1–0, and 2–0 bands near

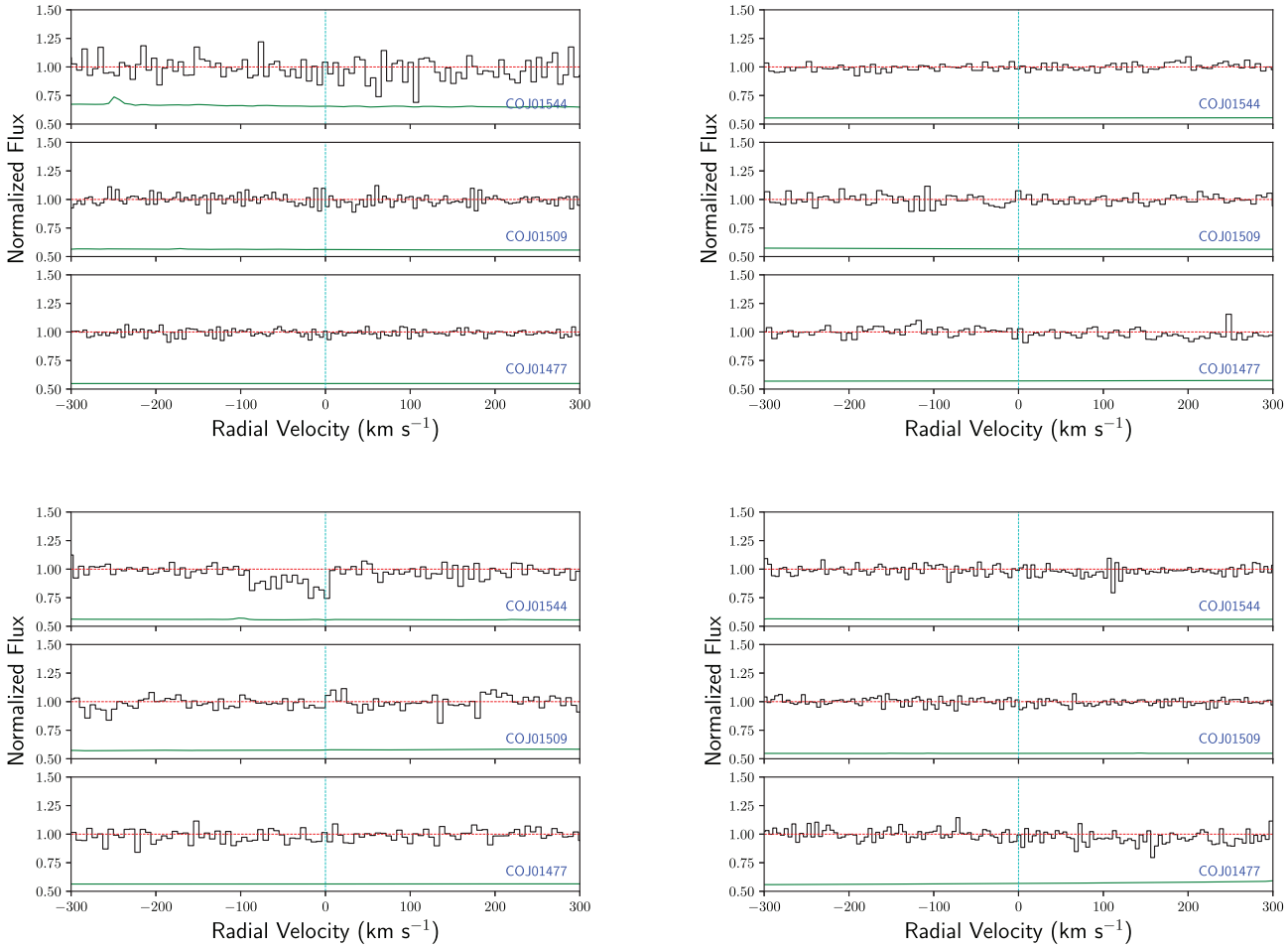

Figure 18. Plot showing the positions of molecular lines of CO for all of the absorbers. The top two plots represent systems at $z = 2.173$ (left-hand panels) and 2.539 (right-hand panels), and the bottom two plots represent systems at $z = 2.635$ (left-hand panels) and 2.236 (right-hand panels), respectively.

Table 12. Limits on column densities of different CO molecular transitions for all the absorbers in this paper.

QSO	z_{abs}	log $N_{CO\,J0\,1544}$	log $N_{CO\,J0\,1509}$	log $N_{CO\,J0\,1477}$
J1106−1731	2.173	<13.87	<13.10	<12.68
J1106−1731	2.539	<13.33	<13.11	<13.08
J1244+1129	2.635	<13.37*	<13.17	<13.03
J1614+1448	2.236	<13.16	<12.71	<12.79

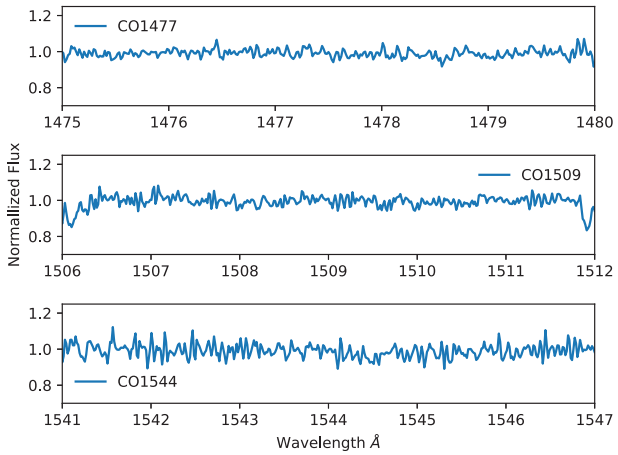

Figure 19. Plot showing the positions of molecular lines of CO after stacking the rest-frame spectra of all the absorbers together.

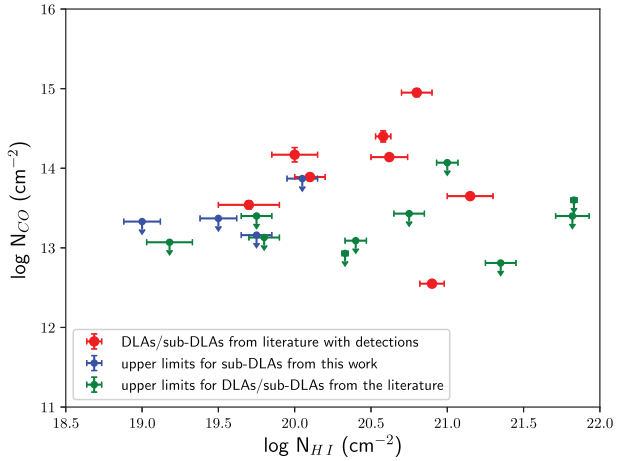

Figure 20. Plot showing the comparison of log $N_{H\,I}$ versus log N_{COJ0} for the sub-DLAs from this work (upper limits) with sub-DLAs/DLAs from literature (including both the limits as well as the detection. The data from literature are compiled from Srianand et al. (2008) and Noterdaeme et al. (2011, 2015, 2017, 2018).

1544, 1510, and 1478 Å. We emphasize the need of higher S/N and lower wavelength spectra of our sub-DLAs to obtain more definitive determinations of H_2 and CO contents.

ACKNOWLEDGEMENTS

We thank an anonymous referee for thoughtful comments that have helped to improved this paper. SP, VPK, and DS thank the helpful staff of Las Campanas Observatory for their assistance during the observing runs. SP and VPK gratefully acknowledge support from NASA grant NNX17AJ26G (PI: Kulkarni) and NSF grant AST-0908890 (PI: Kulkarni). VPK also gratefully acknowledges support from NASA grant 80NSSC20K0887 and NSF grant AST/ 2009811.

DATA AVAILABILITY

The data underlying this paper will be shared on reasonable request to the corresponding author.

REFERENCES

Asplund M., Grevesse N., Sauval A. J., Jacques S. P., 2009, ARA&A, 47, 481
Cashman F. H., Kulkarni V. P., Kisielius R., Ferland G. J., Bogdanovich P., 2017, APJ, 230, 8
Cooke R., Pettini M., Steidel C. C., Rudie G., Nissen P. E., 2011, MNRAS, 417, 1534
Dessauges-Zavadsky M., Peroux C., Kim T. S., DOdorico S., McMahon R. G., 2003, MNRAS, 345, 447
Ferland G. J . et al., 2013, Rev. Mex. Astron. Astrofis., 49, 137
Haehnelt M. G., Steinmetz M., Rauch M., 1998, ApJ, 495, 647
Jorgenson R. A., Murphy M. T., Thompson R., 2013, MNRAS, 435, 482
Khaire V., Srianand R., 2019, MNRAS, 484, 4174
Khare P., Kulkarni V. P., Peŕoux C., York D. G., Lauroesch J. T., Meiring J. D., 2007, A&A, 464, 487
Kulkarni V. P., Fall S. M., 2002, ApJ, 580, 732
Kulkarni V. P., Fall S. M., Lauroesch J. T., York D. G., Welty D. E., Khare P., Truran J. W., 2005, ApJ, 618, 68
Kulkarni V. P., Khare P., Péroux C., York D. G., Lauroesch J. T., Meiring J. D., 2007, ApJ, 661, 88
Kulkarni V. P., Khare P., Som D., Meiring J., York D. G., Péroux C., Lauroesch J. T., 2010, New Astron., 15, 735
Kulkarni V. P . et al., 2012, ApJ, 749, 176
Kulkarni V. P., Som D., Morrison S., Péroux C., Quiret S., York D. G., 2015, ApJ, 815, 24
Ledoux C., Petitjean P., Møller P., Fynbo J., Srianand R., 2006, A&A, 457, 71
Lehner N., Wakker B. P., Savage B. D., 2004, ApJ, 615, 767
Meiring J. D . et al., 2009, MNRAS, 397, 2037
Møller P., Fynbo J. P. U., Ledoux C., Nilsson K. K., 2013, MNRAS, 430, 2680
Morton D. C., 2004, ApJS, 151, 403
Nagamine K., Springel V., Hernquist L., 2004, MNRAS, 348, 421
Nagamine K., Springel V., Hernquist L., 2004, MNRAS, 348, 385
Neeleman M., Prochaska J. X., Wolfe A. M., 2015, ApJ, 800, 7
Noterdaeme P., Petitjean P., Srianand R., Ledoux C., Lopez S., 2011, A&A, 526, L7
Noterdaeme P. et al., 2012, A&A, 547, L1
Noterdaeme P . et al., 2015, A&A, 577, A24
Noterdaeme P. et al., 2017, A&A, 597, A82
Noterdaeme P . et al., 2018, A&A, 612, A58
Nussbaumer H., Storey P. J., 1981, A&A, 96, 91
Penprase B. E., Prochaska J. X., Sargent Wallace L. W., Toro-Martinez I., Beeler D. J., 2010, ApJ, 721, 1
Péroux C., Dessauges-Zavadsky M., D'Odorico S., Kim T.-S., McMahon R. G., 2003a, MNRAS, 345, 480

Pontzen A. et al., 2008, MNRAS, 390, 1349
Pottasch S. R., Wesselius P. R., van Duinen R. J., 1979, A&A, 74, L15
Poudel S., 2020, PhD thesis, Univ. South Carolina
Poudel S., Kulkarni V. P., Morrison S., Péroux C., Som D., Rahmani H., Quiret S., 2018, MNRAS, 473, 3559
Poudel S., Kulkarni V. P., Cashman F. H., Frye B., Péroux C., Rahmani H., Quiret S., 2020, MNRAS, 491, 1008
Prochaska J. X., Wolfe A. M., 1997, ApJ, 487, 73
Prochaska J. X., Gawiser E., Wolfe A. M., Castro S., Djorgovski S. G., 2003a, ApJ, 595, L9
Quiret S. et al., 2016, MNRAS, 458, 4074
Rafelski M., Wolfe A. M., Prochaska J. X., Neeleman M., Mendez A. J., 2012, ApJ, 755, 89
Rafelski M., Neeleman M., Fumagalli M., Wolfe A. M., Prochaska J. X., 2014, ApJ, 782, L29
Savaglio S . et al., 2012, MNRAS, 420, 627
Som D., Kulkarni V. P., Meiring J., York D. G., Péroux C., Khare P., Lauroesch J. T., 2013, MNRAS, 435, 1469
Som D. et al., 2015, ApJ, 806, 25
Srianand R., Petitjean P., 2000, A&A, 357, 414
Srianand R., Petitjean P., Ledoux C., Ferland G., Shaw G., 2005, MNRAS, 362, 549
Srianand R., Gupta N., Petitjean P., Noterdaeme P., Saikia D. J., 2008, MNRAS, 391, L69
Wolfe A. M., Chen H., 2006, ApJ, 652, 981
Wolfe A. M., Prochaska J. X., 1998, ApJ, 494, L15
Wolfe A. M., Gawiser E., Prochaska J. X., 2003, ApJ, 593, 235
Wolfe A. M., Howk J. C., Gawiser E., Prochaska J. X., Lopez S., 2004, ApJ, 615, 625
Wood B. E., Linsky J. L., 1997, ApJ, 474, L39
Wright E. L., 1991, ApJ, 375, 608
Zafar T., Péroux C., Popping A., Milliard B., Deharveng J. M., Frank S., 2013, A&A, 556, A141
Zwaan M., Walter F., Ryan-Weber E., Brinks E., de Blok W. J. G., Kennicutt R. C., 2008, AJ, 136, 2886

This paper has been typeset from a TEX/LATEX file prepared by the author.